LETTER

doi:10.1038/nature16983

Change of carrier density at the pseudogap critical point of a cuprate superconductor

S. Badoux[1], W. Tabis[2,3], F. Laliberté[2], G. Grissonnanche[1], B. Vignolle[2], D. Vignolles[2], J. Béard[2], D. A. Bonn[4,5], W. N. Hardy[4,5], R. Liang[4,5], N. Doiron-Leyraud[1], Louis Taillefer[1,5] & Cyril Proust[2,5]

The pseudogap is a partial gap in the electronic density of states that opens in the normal (non-superconducting) state of cuprate superconductors and whose origin is a long-standing puzzle. Its connection to the Mott insulator phase at low doping (hole concentration, p) remains ambiguous[1] and its relation to the charge order[2–4] that reconstructs the Fermi surface[5,6] at intermediate doping is still unclear[7–10]. Here we use measurements of the Hall coefficient in magnetic fields up to 88 tesla to show that Fermi-surface reconstruction by charge order in the cuprate $YBa_2Cu_3O_y$ ends sharply at a critical doping $p = 0.16$ that is distinctly lower than the pseudogap critical point $p^* = 0.19$ (ref. 11). This shows that the pseudogap and charge order are separate phenomena. We find that the change in carrier density n from $n = 1 + p$ in the conventional metal at high doping (ref. 12) to $n = p$ at low doping (ref. 13) starts at the pseudogap critical point. This shows that the pseudogap and the antiferromagnetic Mott insulator are linked.

Electrons in cuprate materials go from a correlated metallic state at high p to a Mott insulator at $p = 0$. How the system evolves from one state to the other remains a fundamental question. At high doping, the Fermi surface of cuprates is well established. It is a large hole-like cylinder whose volume yields a carrier density $n = 1 + p$, as measured, for example, by quantum oscillations[14], in agreement with band structure calculations. The carrier density can also be measured using the Hall coefficient R_H, because in the limit of $T = 0$ the Hall number n_H of a single-band metal is such that $n_H = n$. Indeed, in the cuprate $Tl_2Ba_2CuO_{6+\delta}$ (Tl-2201), the normal-state Hall coefficient R_H at $p \approx 0.3$, measured at $T \to 0$ in magnetic fields large enough to suppress superconductivity, is such that $n_H = V/(eR_H) \approx 1 + p$, where e is the electron charge and V the volume per Cu atom in the CuO_2 planes[12,15].

By contrast, at low doping, measurements of R_H in $La_{2-x}Sr_xCuO_4$ (LSCO) (ref. 13) and $YBa_2Cu_3O_y$ (YBCO) (ref. 16) yield $n_H \approx p$, below $p \approx 0.08$. Having a carrier density equal to the hole concentration, $n = p$, is known to be an experimental signature of the lightly doped cuprates. The question is: at what doping does the transition between those two limiting regimes take place? Specifically, does the transition from $n = 1 + p$ to $n = p$ occur at p^*, the critical doping for the onset of the pseudogap phase? The pseudogap is a partial gap in the normal-state density of states that appears below $p^* \approx 0.19$ (ref. 11), and whose origin is a central puzzle in the physics of correlated electrons and the subject of much debate.

To answer this question using Hall measurements, one needs to reach low temperatures, which requires the use of large magnetic fields to suppress superconductivity. The only prior high-field study of cuprates that goes across p^* was performed on LSCO (ref. 17), a cuprate superconductor with a relatively low critical temperature ($T_c < 40$ K) and critical field ($H_{c2} < 60$ T). For mainly two reasons, studies on LSCO were inconclusive on the transition from $n = 1 + p$ to $n = p$. First, the Fermi surface of overdoped LSCO undergoes a Lifshitz transition from a hole-like to an electron-like surface as its band structure crosses a saddle-point van Hove singularity at $p \approx 0.2$ (ref. 18). This transition causes large changes in $R_H(T)$ (ref. 15) that can mask the effect of the pseudogap onset at $p^* \approx 0.19$. The second reason is the ill-defined impact of the charge-density-wave (CDW) modulations that develop at low temperature in a doping range near $p \approx 0.12$ (ref. 19). Such CDW modulations should cause a reconstruction of the Fermi surface, and hence change R_H at low temperature[6]. Therefore, the anomalies in n_H versus p observed below 60 K in LSCO (ref. 17)—and in $Bi_2La_{2-x}Sr_xCuO_{6+\delta}$ (ref. 20)—between $p \approx 0.1$ and $p \approx 0.2$ are most likely to be the combined result of three effects that have yet to be disentangled: Lifshitz transition, Fermi-surface reconstruction (FSR) and pseudogap.

Here we turn to YBCO, a cuprate material with several advantages. First, it is one of the cleanest and best ordered of all cuprates, thereby ensuring a homogeneous doping ideal for distinguishing nearby critical points. Second, the location of the pseudogap critical point is well established in YBCO, at $p^* = 0.19 \pm 0.01$ (ref. 11). Third, the Lifshitz transition in YBCO occurs at $p > 0.29$ (ref. 21), well above p^*. Fourth, the CDW modulations in YBCO have been thoroughly characterized. They are detected by X-ray diffraction (XRD) between $p \approx 0.08$ and $p \approx 0.16$ (refs 22, 23), below a temperature T_{XRD} (Fig. 1a). Above a threshold magnetic field, CDW order is detected by NMR (refs 2, 24) below a temperature T_{NMR} (Fig. 1b). Fifth, the FSR caused by the CDW modulations has a well-defined signature in the Hall effect of YBCO: $R_H(T)$ decreases smoothly to become negative at low temperature[6]—the signature of an electron pocket in the reconstructed Fermi surface. Prior Hall measurements in magnetic fields up to 60 T show that the CDW-induced FSR begins sharply at $p = 0.08$ and persists up to $p = 0.15$, the highest doping reached so far[6].

YBCO has one disadvantage, however. Its orthorhombic structure contains conducting CuO chains along the b axis, which reduce the Hall signal coming from the CuO_2 planes. While this has no impact on the qualitative features of $R_H(T)$ (such as its sign or its qualitative T dependence), it does modify the quantitative relation between the measured Hall number n_H and the inferred carrier density n. Specifically, $n = (\rho_b/\rho_a)n_H$ (ref. 16), where ρ_b and ρ_a are the in-plane resistivities parallel and perpendicular to the b axis, respectively (see Methods and Extended Data Fig. 1).

We have performed Hall measurements in YBCO up to 88 T, allowing us to extend the doping range upwards, and hence track the normal-state properties across p^*, down to at least $T = 40$ K. Our complete data on four YBCO samples with dopings $p = 0.16$, 0.177, 0.19 and 0.205 are displayed in Extended Data Figs 2, 3, 4 and 5, respectively. In Fig. 2, we compare field sweeps of R_H versus H at $p = 0.15$ (Fig. 2a; from ref. 6) and $p = 0.16$ (Fig. 2b), at various temperatures down to 25 K. The difference is striking. At $p = 0.15$, the high-field isotherms $R_H(H)$ drop monotonically with decreasing T until they become negative at low T.

[1]Département de physique, Regroupement Québécois sur les Matériaux de Pointe, Université de Sherbrooke, Sherbrooke, Québec J1K 2R1, Canada. [2]Laboratoire National des Champs Magnétiques Intenses (CNRS, EMFL, INSA, UGA, UPS), Toulouse 31400, France. [3]AGH University of Science and Technology, Faculty of Physics and Applied Computer Science, 30-059 Krakow, Poland. [4]Department of Physics and Astronomy, University of British Columbia, Vancouver, British Columbia V6T 1Z1, Canada. [5]Canadian Institute for Advanced Research, Toronto, Ontario M5G 1Z8, Canada.

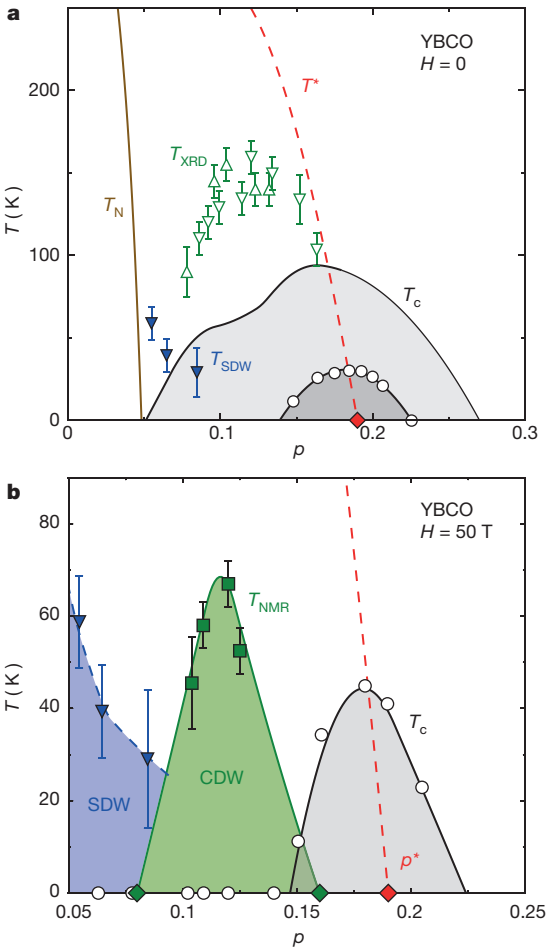

Figure 1 | Temperature–doping phase diagram of YBCO. a, Phase diagram in zero magnetic field ($H = 0$). The superconducting phase (grey dome) lies below T_c (solid black line) and the antiferromagnetic phase lies below T_N (brown line). The small (dark grey) dome shows how T_c is suppressed by substituting 6% of the Cu atoms for Zn (white circles from ref. 25). Short-range charge-density-wave (CDW) modulations are detected by X-ray diffraction below T_{XRD} (upward-pointing open triangles and error bars from ref. 22; downward-pointing open triangles and error bars from ref. 23). Note that unlike T_{XRD}, the amplitude of the CDW modulations decreases monotonically to zero as doping goes from $p = 0.12$ to $p_{CDW} = 0.16 \pm 0.005$ (refs 22, 23). Short-range spin-density-wave (SDW) modulations are detected by neutron diffraction below T_{SDW} (blue triangles and error bars[28]). The red dashed line marks the approximate location of the pseudogap temperature T^*, while $p^* = 0.19 \pm 0.01$ marks the critical doping below which the pseudogap is known to appear[11] (red diamond). **b**, Phase diagram in a magnetic field of $H = 50$ T. Above a threshold magnetic field, CDW order is detected by NMR (ref. 2) below a transition temperature T_{NMR} (green squares and error bars[24]). The green region is where the Hall coefficient R_H is negative (from ref. 6 and this work), starting above $p = 0.08$ (left green diamond). Our Hall data show that Fermi-surface reconstruction, and hence CDW order, ends at $p_{FSR} = 0.16 \pm 0.005$ (right green diamond). The red dashed line is the same as in **a**. The zero-field SDW phase is reproduced from **a** (blue region). The black and green solid lines and the blue dashed line are guides to the eye.

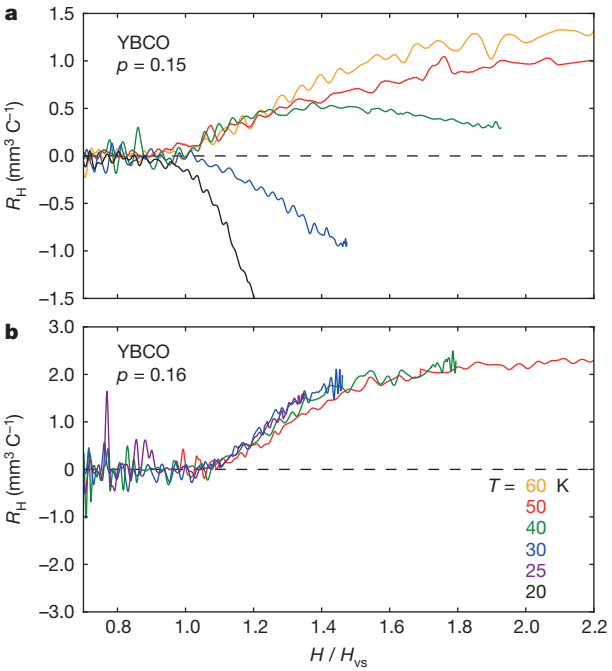

Figure 2 | Field dependence of the Hall coefficient in YBCO. a, **b**, Hall coefficient (R_H) of YBCO at various fixed temperatures, as indicated, plotted as R_H versus H/H_{vs}, where $H_{vs}(T)$ is the vortex-solid melting field above which R_H becomes non-zero, for two dopings: $p = 0.15$ (**a**) and $p = 0.16$ (**b**). Upon cooling, we see that R_H decreases and eventually becomes negative at $p = 0.15$, while it never drops at $p = 0.16$.

At $p = 0.16$, $R_H(H)$ never drops. Figure 3 compares the temperature evolution of the normal-state R_H at different dopings. In Fig. 3a, we see that $R_H(T)$ at $p = 0.16$ shows no sign of the drop to negative values displayed at $p = 0.12$, 0.135 and 0.15, at least down to $T = 40$ K. Having said this, and although the isotherms at $T = 25$ K and 30 K are consistent with a constant R_H below $T = 50$ K (Fig. 2), we cannot exclude that $R_H(T)$ might drop below 40 K. However, even if it did, the onset temperature for FSR would have to be much lower than it is at $p = 0.15$, and it would extrapolate to zero at $p < 0.165$ (Extended Data Fig. 6). We therefore find that the critical doping above which there is no FSR in the normal state of YBCO at $T = 0$ is $p_{FSR} = 0.16 \pm 0.005$. Because this is in excellent agreement with the maximal doping at which short-range CDW modulations have been detected by XRD, namely $p_{XRD} = 0.16 \pm 0.005$ (refs 22, 23), and it is consistent with the region of CDW order seen by NMR (ref. 24) (Fig. 1b), we conclude that the critical doping where CDW order ends in YBCO is $p_{CDW} = 0.16 \pm 0.005$. This is consistent with the highest doping at which quantum oscillations from the CDW-induced electron pocket have been detected, namely $p = 0.152$ (ref. 9).

An onset of CDW order at $p_{CDW} = 0.16$ is distinctly lower than the onset of the pseudogap. Indeed, extensive analysis of the normal-state properties of YBCO above T_c yields $p^* = 0.19 \pm 0.01$ (ref. 11). The critical point p^* can also be located by suppressing superconductivity with 6% Zn impurities[25], which shrinks the T_c dome to a small region centred around $p^* = 0.19$ (Fig. 1a). This robustness of p^* confirms that CDW order and pseudogap are distinct phenomena, since CDW modulations are rapidly weakened by Zn substitution[26]. Applying a field of 50 T produces a small T_c dome peaked at exactly the same doping, showing that $p^* = 0.19 \pm 0.01$ in the normal state, whether induced by Zn or by field (Fig. 1).

We have arrived at our first main finding: the onset of pseudogap and CDW order occurs at two distinct and well-separated critical dopings. Just as $T_{XRD} < T^*$ (and $T_{NMR} < T^*$) (Fig. 1), we now find that $p_{CDW} < p^*$, in the normal state of YBCO. This contrasts with the simultaneous onset of pseudogap and short-range CDW modulations observed in the zero-field superconducting state of $Bi_2Sr_2CaCuO_{8+x}$ (Bi-2212) by scanning tunnelling microscopy (ref. 8).

Having established that the FSR due to CDW order ends at $p_{FSR} = 0.16$, we now see what happens at higher p. At $p = 0.205$, the temperature dependence of R_H in YBCO is similar to that of Tl-2201 (refs 12, 15) at dopings where the Fermi surface is known to be a single large hole-like cylinder with carrier density $n = 1 + p$ (refs 14, 15) (Extended Data Fig. 7). In particular, as T increases from zero, $R_H(T)$ rises initially, because of the growth in inelastic scattering, which is anisotropic around the large Fermi surface[15]. This yields a characteristic

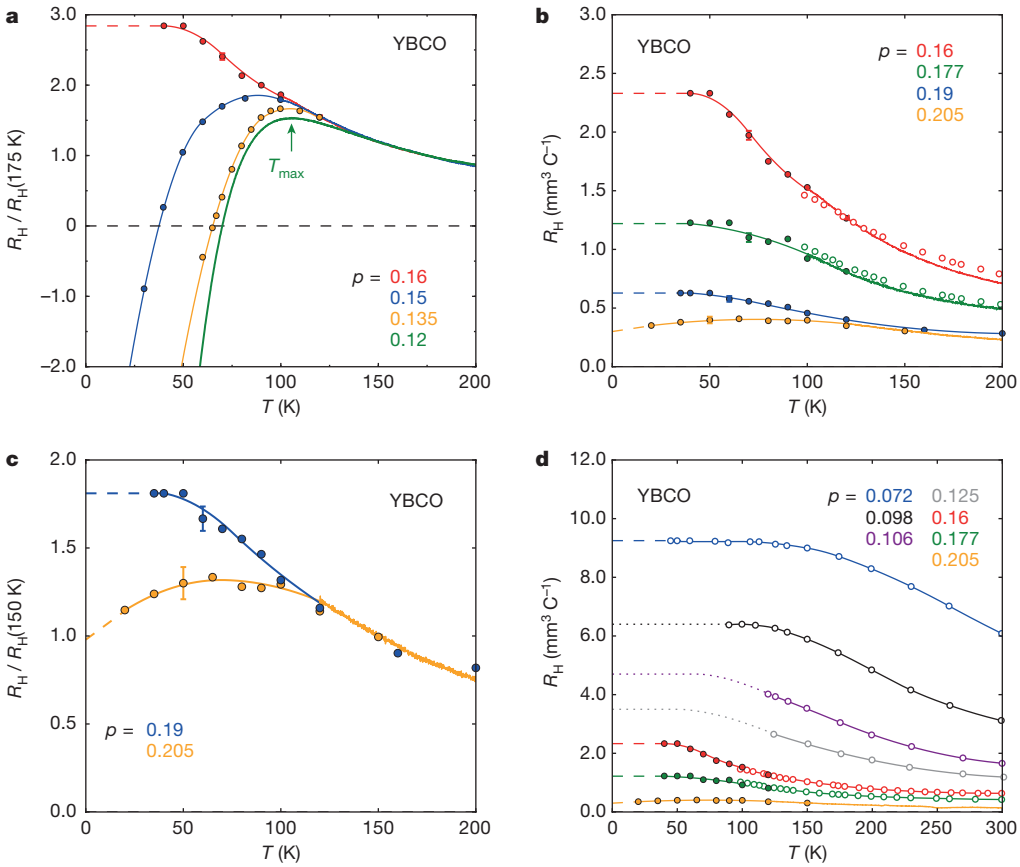

Figure 3 | Temperature dependence of the normal-state Hall coefficient in YBCO at various dopings. a, Data points (circles), R_H normalized by its value at $T = 175$ K. The solid curves are temperature sweeps at $H = 16$ T, above $T = 100$ K (red), 100 K (blue), 120 K (yellow) and 60 K (green). Solid lines are guides through the data points, below 100 K (red and blue) and 120 K (yellow). The red dashed line is a flat extrapolation below 40 K. The data points for $p = 0.16$ (red) are taken at (or extrapolated to) $H = 80$ T, from the R_H versus H isotherms in Extended Data Fig. 2. The data points for $p = 0.15$ (blue) and $p = 0.135$ (yellow) are taken from ref. 6 (at $H = 55$ T). The arrow marks the location of the peak in R_H versus T, for $p = 0.12$ (T_{max}). The drop in $R_H(T)$ at low temperature is the signature of Fermi-surface reconstruction (FSR), caused by charge-density-wave (CDW) order. At $p = 0.16$, no such drop occurs, at least down to 40 K. This reveals that the critical doping for the end of FSR in the doping phase diagram (Fig. 1b) is $p_{FSR} = 0.16 \pm 0.005$ (Extended Data Fig. 6). **b**, R_H versus T at $p = 0.16$ and higher, measured at (or extrapolated to) $H = 80$ T (filled circles), from isotherms in Extended Data Figs 2, 3, 4 and 5. The curves are temperature sweeps at $H = 16$ T, above $T = 100$ K (red), 100 K (green), 120 K (yellow). Colour-coded lines are a guide to the eye through the data points. The dashed lines are a linear extrapolation below the lowest data point. Open circles are low-field data from ref. 16 for the normal-state $R_H(T)$ of YBCO above T_c, for $p = 0.16$ (red, $y = 6.95$, $T_c = 93$ K) and $p = 0.178$ (green, $y = 7.00$, $T_c = 91$ K). These data are in excellent quantitative agreement with our own data. The error bars reflect the relative uncertainty in determining the change in R_H versus T for a given doping (see Methods). Shown only for one data point per doping, the colour-coded error bar is the same for all points on the corresponding curve (doping). **c**, Same as **b** showing the two highest dopings only, but with R_H normalized at $T = 150$ K. The curve at $p = 0.19$ is qualitatively different from the curve at $p = 0.205$, showing no sign of a drop at low T (Extended Data Fig. 8). We attribute the twofold increase in the magnitude of R_H at $T \to 0$ to a decrease in carrier density as the pseudogap opens at p^*, with p^* located between $p = 0.205$ and $p = 0.19$. **d**, Same as **b** but over a wider range of doping and temperature. For the three curves in the interval $0.09 < p < 0.15$, the dotted lines show how the normal-state $R_H(T)$ might extend down to $T = 0$ in the absence of the FSR caused by CDW order.

peak in $R_H(T)$, at $T \approx 100$ K (Extended Data Fig. 7). Moving to $p = 0.19$, a qualitative change has taken place (Fig. 3c): $R_H(T)$ now shows no sign of a decrease as $T \to 0$, down to our lowest temperature of 35 K (Extended Data Fig. 8). The extrapolated $T = 0$ value, $R_H(0)$, doubles upon crossing p^*.

Moving to still lower doping, we see that there is also a major quantitative change: the magnitude of R_H at low T undergoes a nearly sixfold increase between $p = 0.205$ and $p = 0.16$ (Fig. 3b), seen directly in the raw data at $T = 50$ K (Fig. 4a). We attribute this huge increase in R_H to a corresponding decrease in carrier density. In other words, states at the Fermi surface are lost and $R_H(T = 0)$ increases. One may argue that for $p < 0.2$ $R_H(T)$ could decrease below 50 K and reach a value at $T = 0$ such that $n_H = 1 + p$ for all dopings down to $p = 0.16$. In this scenario, the peak in $R_H(T)$ at $T = 50$ K would be due to an anisotropic inelastic scattering that grows rapidly with underdoping[15]. In Methods and Extended Data Fig. 9, we show that this mechanism is inconsistent with the measured resistivity of YBCO, which is essentially independent of doping at $T = 50$ K (Extended Data Fig. 9).

In Fig. 4b, we plot n_H versus p and discover that in the normal state of YBCO the transition from the conventional metal at high p (where $n_H = 1 + p$) to the lightly doped regime at low p (where $n_H = p$) starts sharply at $p = p^*$, where the pseudogap opens. This is our second main finding. The observed change in R_H by a factor of $\sim$6 is now understandable, since $(1 + p^*)/p^* = 6.3$. It is important to note that the huge rise in $R_H(0)$ as p is reduced below p^* is the result of a gradual process that begins at high temperature. As seen in Fig. 3d, the order-of-magnitude growth in R_H with decreasing p seen at $T \to 0$ is also observed at 300 K. Moreover, this growth is monotonic. Those two facts are consistent with the pseudogap phase, whose characteristic temperature T^* rises monotonically with decreasing p, to values exceeding 300 K (Fig. 1a). By contrast, CDW modulations cannot be responsible for the enhanced $R_H(T)$, since their onset temperature is non-monotonic and it never exceeds 150 K (Fig. 1a).

In the pseudogap phase, the topology of the $T = 0$ Fermi surface in the absence of superconductivity and CDW order is unknown. However, because the pseudogap opens at reciprocal-space locations

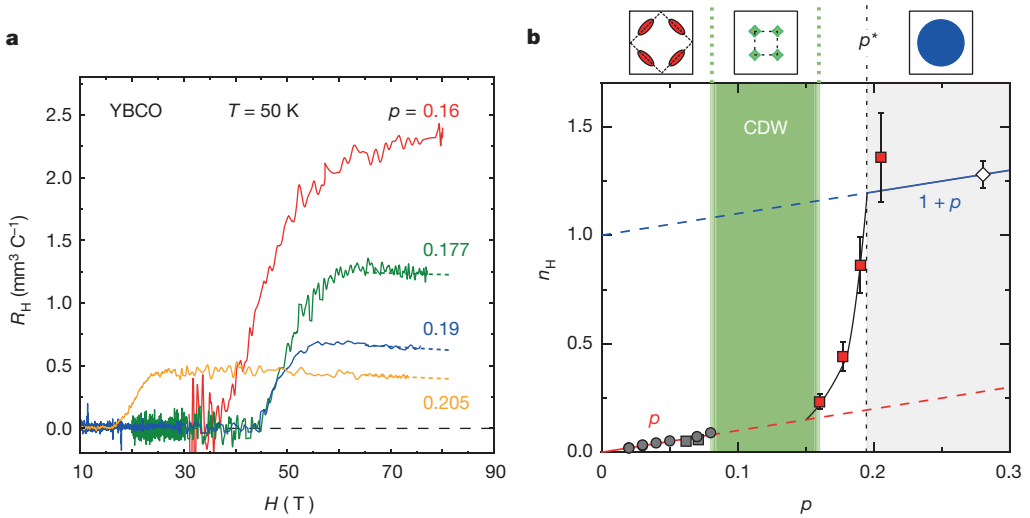

Figure 4 | Doping evolution of the normal-state carrier density. **a**, Isotherms of R_H versus H in YBCO at $p = 0.16$, 0.177, 0.19 and 0.205, measured at $T = 50$ K. Note the huge increase in the value of R_H at $H = 80$ T (or extrapolated to $H = 80$ T; dashed lines), by a factor 5.7, when going from $p = 0.205$ to $p = 0.16$. **b**, Doping dependence of the Hall number, $n_H = V/(eR_H)$, in hole-doped cuprates, measured in the normal state at $T = 50$ K for LSCO (circles, ref. 13) and YBCO ($p < 0.08$, grey squares, ref. 16). For YBCO at $p > 0.15$ (red squares), we use R_H at $H = 80$ T from **a**. The white diamond (with its error bar) is obtained from the $T = 0$ limit of $R_H(T)$ in strongly overdoped Tl-2201 (ref. 12). The solid black line is a guide to the eye. The red line is $n_H = p$; the blue line is $n_H = 1 + p$. The region where Fermi-surface reconstruction due to CDW order occurs in YBCO is marked as a green band; in that band, $R_H < 0$ at $T \to 0$. The error bars (±15%) for our four samples (red squares) reflect the uncertainty in measuring the geometric factor (see Methods). In YBCO, the carrier density is given by $n = n_H/(\rho_a/\rho_b)$, where ρ_a/ρ_b is the anisotropy ratio of the in-plane resistivity[16]. For our samples, $\rho_a/\rho_b \approx 1.5$ (see Methods and Extended Data Fig. 1), so that $n \approx p$ at $p = 0.16$. With decreasing p, the carrier density is seen to drop rapidly from $1 + p$ to p at $p^* = 0.19 \pm 0.01$ (black dotted line), the critical doping for the onset of the pseudogap in YBCO (ref. 11; Fig. 1). The icons above the figure show a sketch of the normal-state Fermi surface in three of the four doping regions: small nodal hole pockets (red) below $p = 0.08$, where magnetic order prevails at low temperature (Fig. 1); small electron pockets (green) between $p = 0.08$ and $p = 0.16$, where charge order (CDW) prevails at low temperature (Fig. 1b); a single large hole surface (blue) above p^*, where the non-superconducting ground state is a correlated metal (grey region).

$k = (0, \pm\pi)$ and $(\pm\pi, 0)$, the electronic states at the Fermi level must lie near $k = (\pm\pi/2, \pm\pi/2)$, where the four nodes of the d-wave superconducting gap are located. This is indeed what is observed, in the form of nodal Fermi arcs, for example by ARPES (angle-resolved photoemission spectroscopy) in YBCO (ref. 21) and by scanning tunnelling microscopy in Bi-2212 (ref. 8), below $p \approx 0.2$. Given that the relation $n_H = p$ extends down to the lowest dopings (Fig. 4b), two scenarios for these nodal states come to mind. One is associated with the antiferromagnetic order, the other is associated with the Mott insulator.

In the first scenario, antiferromagnetic order with a commensurate wavevector $Q = (\pi, \pi)$—the order that prevails in YBCO below $p = 0.05$ (Fig. 1a)—would reconstruct the large Fermi surface into four small hole-like nodal pockets whose total volume would contain p carriers, so that $n_H = p$ (see sketch in Fig. 4b). In electron-doped cuprates, an antiferromagnetic quantum critical point is believed to account for the abrupt drop in carrier density detected in the normal-state Hall coefficient[27]. The question is whether in YBCO magnetic order—present at low temperature up to $p \approx 0.08$ in zero field[28] (Fig. 1b)—could extend up to $p^* = 0.19$ when superconductivity is suppressed by a magnetic field of the order of 100 T. An antiferromagnetic quantum critical point at p^* in YBCO could account for the linear temperature dependence of the resistivity[29] and possibly also the divergent effective mass[9].

In the second scenario, the pseudogap phase is a consequence of strong correlations associated with Mott physics. Numerical solutions of the Hubbard model find nodal Fermi arcs at low doping and intermediate temperatures[30,31]. It has been argued that at $T \to 0$, the Fermi surface could in fact consist of four hole-like nodal pockets[32,33] whose total volume would contain p carriers. These arcs/pockets develop even though translational symmetry is not broken. The question is whether such a Mott-based pseudogap can appear at a doping as high as $p = 0.19$.

Overall, the fact that the normal-state carrier density—measured directly in the archetypal cuprate YBCO at low temperature—drops sharply from $n = 1 + p$ to $n = p$ precisely at p^* reveals a robust and fundamental new fact about the pseudogap phase: it causes a transformation of the Fermi surface such that its volume suddenly shrinks by one hole per Cu atom. We expect that a microscopic understanding of this transformation will elucidate the enigmatic behaviour of electrons in cuprate superconductors.

Online Content Methods, along with any additional Extended Data display items and Source Data, are available in the online version of the paper; references unique to these sections appear only in the online paper.

Received 22 October 2015; accepted 5 January 2016.
Published online 22 February 2016.

1. Norman, M. R., Pines, D. & Kallin, C. The pseudogap: friend or foe of high T_c? *Adv. Phys.* **54,** 715–733 (2005).
2. Wu, T. *et al.* Magnetic-field-induced charge-stripe order in the high-temperature superconductor $YBa_2Cu_3O_y$. *Nature* **477,** 191–194 (2011).
3. Ghiringhelli, G. *et al.* Long-range incommensurate charge fluctuations in $(Y,Nd)Ba_2Cu_3O_{6+x}$. *Science* **337,** 821–825 (2012).
4. Chang, J. *et al.* Direct observation of competition between superconductivity and charge density wave order in $YBa_2Cu_3O_{6.67}$. *Nature Phys.* **8,** 871–876 (2012).
5. Doiron-Leyraud, N. *et al.* Quantum oscillations and the Fermi surface in an underdoped high-T_c superconductor. *Nature* **447,** 565–568 (2007).
6. LeBoeuf, D. *et al.* Lifshitz critical point in the cuprate superconductor $YBa_2Cu_3O_y$ from high-field Hall effect measurements. *Phys. Rev. B* **83,** 054506 (2011).
7. He, Y. *et al.* Fermi surface and pseudogap evolution in a cuprate superconductor. *Science* **344,** 608–611 (2014).
8. Fujita, K. *et al.* Simultaneous transitions in cuprate momentum-space topology and electronic symmetry breaking. *Science* **344,** 612–616 (2014).
9. Ramshaw, B. J. *et al.* Quasiparticle mass enhancement approaching optimal doping in a high-T_c superconductor. *Science* **348,** 317–320 (2015).
10. Senthil, T. On the mass enhancement near optimal doping in high magnetic fields in the cuprates. Preprint at http://arXiv.org/abs/1410.2096 (2014).
11. Tallon, J. L. & Loram, J. W. The doping dependence of T^* — what is the real high-T_c phase diagram? *Physica C* **349,** 53–68 (2001).
12. Mackenzie, A. P. *et al.* Normal-state magnetotransport in superconducting $Ta_2Ba_2CuO_{6+\delta}$ to millikelvin temperatures. *Phys. Rev. B* **53,** 5848–5855 (1996).
13. Ando, Y. *et al.* Evolution of the Hall coefficient and the peculiar electronic structure of the cuprate superconductors. *Phys. Rev. Lett.* **92,** 197001 (2004).

14. Vignolle, B. *et al.* Quantum oscillations in an overdoped high-T_c superconductor. *Nature* **455,** 952–955 (2008).
15. Hussey, N. E. Phenomenology of the normal state in-plane transport properties of high-T_c cuprates. *J. Phys. Condens. Matter* **20,** 123201 (2008).
16. Segawa, K. & Ando, Y. Intrinsic Hall response of the CuO_2 planes in a chain-plane composite system of $YBa_2Cu_3O_y$. *Phys. Rev. B* **69,** 104521 (2004).
17. Balakirev, F. F. *et al.* Quantum phase transition in the magnetic-field-induced normal state of optimum-doped high-T_c cuprate superconductors at low temperatures. *Phys. Rev. Lett.* **102,** 017004 (2009).
18. Yoshida, T. *et al.* Systematic doping evolution of the underlying Fermi surface of $La_{2-x}Sr_xCuO_4$. *Phys. Rev. B* **74,** 224510 (2006).
19. Croft, T. P., Lester, C., Senn, M. S., Bombardi, A. & Hayden, S. M. Charge density wave fluctuations in $La_{2-x}Sr_xCuO_4$ and their competition with superconductivity. *Phys. Rev. B* **89,** 224513 (2014).
20. Balakirev, F. F. *et al.* Signature of optimal doping in Hall-effect measurements on a high-temperature superconductor. *Nature* **424,** 912–915 (2003).
21. Fournier, D. *et al.* Loss of nodal quasiparticle integrity in underdoped $YBa_2Cu_3O_{6+x}$. *Nature Phys.* **6,** 905–911 (2010).
22. Hücker, M. *et al.* Competing charge, spin and superconducting orders in underdoped $YBa_2Cu_3O_y$. *Phys. Rev. B* **90,** 054514 (2014).
23. Blanco-Canosa, S. *et al.* Resonant X-ray scattering study of charge-density wave correlations in $YBa_2Cu_3O_{6+x}$. *Phys. Rev. B* **90,** 054513 (2014).
24. Wu, T. *et al.* Emergence of charge order from the vortex state of a high-temperature superconductor. *Nature Commun.* **4,** 2113 (2013).
25. Tallon, J. L. *et al.* Zn-induced T_c reduction in high-T_c superconductors: scattering in the presence of a pseudogap. *Phys. Rev. Lett.* **79,** 5294–5297 (1997).
26. Blanco-Canosa, S. *et al.* Momentum-dependent charge correlations in $YBa_2Cu_3O_{6+\delta}$ superconductors probed by resonant X-ray scattering: evidence for three competing phases. *Phys. Rev. Lett.* **110,** 187001 (2013).
27. Dagan, Y. *et al.* Evidence for a quantum phase transition in $Pr_{2-x}Ce_xCuO_{4-\delta}$ from transport measurements. *Phys. Rev. Lett.* **92,** 167001 (2004).
28. Haug, D. *et al.* Neutron scattering study of the magnetic phase diagram of underdoped $YBa_2Cu_3O_{6+x}$. *New J. Phys.* **12,** 105006 (2010).
29. Taillefer, L. Scattering and pairing in cuprate superconductors. *Annu. Rev. Condens. Matter Phys.* **1,** 51–70 (2010).
30. Sénéchal, D. & Tremblay, A.-M. S. Hot spots and pseudogaps for hole- and electron-doped high-temperature superconductors. *Phys. Rev. Lett.* **92,** 126401 (2004).
31. Ferrero, M. *et al.* Pseudogap opening and formation of Fermi arcs as an orbital-selective Mott transition in momentum space. *Phys. Rev. B* **80,** 064501 (2009).
32. Rice, T. M. *et al.* A phenomenological theory of the anomalous pseudogap phase in underdoped cuprates. *Rep. Prog. Phys.* **75,** 016502 (2012).
33. Chowdhury, D. & Sachdev, S. Density-wave instabilities of fractionalized Fermi liquids. *Phys. Rev. B* **90,** 245136 (2014).

Acknowledgements We thank the following for discussions: Y. Ando, D. Basov, G. Boebinger, C. Bourbonnais, J. P. Carbotte, A. Carrington, J. Chang, A. V. Chubukov, J. C. Davis, A. Georges, N. E. Hussey, M.-H. Julien, H.-Y. Kee, S. A. Kivelson, P. A. Lee, T. Loew, G. G. Lonzarich, W. Metzner, A. J. Millis, M. R. Norman, C. Pépin, J. Porras, B. J. Ramshaw, T. M. Rice, G. Rikken, S. Sachdev, D. J. Scalapino, C. B. Taillefer, J. L. Tallon, S. Todadri, and A.-M. S. Tremblay. We also thank P. Frings and J.P. Nicolin for help during the measurements in Toulouse. L.T. thanks the Laboratoire National des Champs Magnétiques Intenses (LNCMI) in Toulouse for their hospitality and LABEX NEXT for their support while this work was being performed. A portion of this work was performed at the LNCMI, which is supported by the French ANR SUPERFIELD, the EMFL, and the LABEX NEXT. R.L., D.A.B. and W.N.H. acknowledge funding from the Natural Sciences and Engineering Research Council of Canada (NSERC). L.T. acknowledges support from the Canadian Institute for Advanced Research (CIFAR) and funding from NSERC, the Fonds de recherche du Québec – Nature et Technologies (FRQNT), the Canada Foundation for Innovation (CFI) and a Canada Research Chair.

Author Contributions S.B., W.T., F.L., B.V., D.V., J.B. and C.P. performed the transport measurements at the LNCMI. S.B. and N.D.-L. performed the transport measurements at Sherbrooke. G.G. performed the calculations of the transport coefficients. D.A.B., W.N.H. and R.L. prepared the YBCO single crystals at UBC. S.B., L.T. and C.P. wrote the manuscript, in consultation with all authors. L.T. and C.P. co-supervised the project.

Author Information Reprints and permissions information is available at www.nature.com/reprints. The authors declare no competing financial interests. Readers are welcome to comment on the online version of the paper. Correspondence and requests for materials should be addressed to L.T. (louis.taillefer@usherbrooke.ca) or C.P. (cyril.proust@lncmi.cnrs.fr).

METHODS

Samples. Single crystals of $YBa_2Cu_3O_y$ (YBCO) were obtained by flux growth at UBC (ref. 34). The superconducting transition temperature T_c was determined as the temperature below which the zero-field resistance $R=0$. The hole doping p is obtained from T_c (ref. 35). In order to access dopings above $p=0.18$, Ca substitution was used, at the level of 1.4% (giving $p=0.19$) and 5% (giving $p=0.205$). The samples are rectangular platelets with six contacts applied in the standard geometry, using diffused gold pads.

Measurement of the longitudinal and transverse resistances. The longitudinal resistance R_{xx} and transverse (Hall) resistance R_{xy} of our YBCO samples were measured in Sherbrooke in steady fields up to 16 T and in Toulouse in pulsed fields up to 88 T, using a dual coil magnet developed at the LNCMI-Toulouse to produce non-destructive magnetic fields up to 90 T. The magnetic field profile is shown in Extended Data Fig. 10.

The pulsed-field measurements were performed using a conventional six-point configuration with a current excitation between 5 mA and 10 mA at a frequency of ~60 kHz. A high-speed acquisition system was used to digitize the reference signal (current) and the voltage drop across the sample at a frequency of 500 kHz. The data were post-analysed with software to perform the phase comparison. Data for the rise and fall of the field pulse were in good agreement, thus excluding any heating due to eddy currents. Tests at different frequencies showed excellent reproducibility.

Error bars. Note that the resistance of the samples was small due to their geometric factor and their high conductivity in this doping range — typically a few milliohms in the normal state at high fields. Despite the fact that R_{xy} was obtained by anti-symmetrizing the signals measured for a field parallel and anti-parallel to the c axis, a slight negative slope was observed in the Hall coefficient R_H versus H, similar to that found in prior high-field studies[17,20]. This slope, which may be intrinsic or not, has no impact on any of our conclusions, since they do not depend on the precise absolute value of R_H. Indeed, our conclusions depend on two results: (1) the temperature dependence of R_H at low T, in a given sample; (2) the doping dependence of R_H at low T, at a given temperature. In both cases, what matters is to measure R_H at the same value of H, namely $H=80$ T. So in Fig. 3c, and Extended Data Figs 7 and 8, where we compare the detailed temperature dependence of $R_H(T)$ in two samples ($p=0.19$ and $p=0.205$), the relevant uncertainty is the relative error bar associated with a change of temperature in one sample. That error is defined as the standard deviation of the value of R_H at $H=80$ T given by the linear fit in Extended Data Fig. 8. The maximum such error bar is shown in Fig. 3 for each of our four samples.

In Fig. 4a, we simply compare the magnitude of R_H in our four samples when measured at $H=80$ T and $T=50$ K. As can be seen from the raw data, the negative slope of R_H versus H does not really affect this comparison. What is involved is the error bar on the absolute value of R_H (in $mm^3\,C^{-1}$), which involves geometric factors and which we estimate to be at most ±15%. This error bar is shown in Fig. 4b. Note the excellent quantitative agreement between our data and the data of ref. 16 at $p=0.16$ and 0.177 (Fig. 3b).

Sample size. No statistical methods were used to predetermine sample size.

Relation between Hall number and carrier density in YBCO. In Fig. 4b, we plot the Hall number $n_H=V/(eR_H)$. In YBCO, the relation between n_H and the carrier density n involves a correction factor, the in-plane anisotropy of transport, so that $n=n_H/(\rho_a/\rho_b)$, where ρ_a and ρ_b are the resistivities along the a and b directions of the orthorhombic structure, respectively. This is because the conducting CuO chains that run along the b axis short-circuit the transverse (Hall) voltage when a current is sent along the a axis[16].

In Extended Data Fig. 1, we show the chain resistivity ρ_{chain} of our YBCO sample at $p=0.177$, defined as $\rho_{chain}=1/(1/\rho_b-1/\rho_a)$. It displays the known T^2 behaviour of chain conduction[36], with $\rho_{chain}=50\ \mu\Omega$ cm at $T=50$ K. Combined with the $\rho_a(T)$ data plotted in Extended Data Fig. 9, where $\rho_a=25\ \mu\Omega$ cm at $T=50$ K, we get $\rho_a/\rho_b=1.5$ at $T=50$ K. We expect a similar anisotropy for the four samples used in our study.

Therefore, if in Fig. 4b we wanted to plot n instead of n_H, we would need to divide n_H by 1.5. The red squares at $p=0.16$, 0.177 and 0.19 would move down by a factor of 1.5. For $p=0.16$, this means that $n\approx p$, since $n_H\approx 0.24$. So our claim that $n\approx p$ below p^* remains correct. For $p=0.205$, we get $n\approx 0.9$, significantly below $1+p=1.205$. However, at $p=0.205$, the value of n_H at $T=0$ is larger than at $T=50$ K (Fig. 3c), by a factor of 1.3 or so, giving $n(T\to 0)\approx 1.2$.

Calculation of the Hall coefficient and resistivity in cuprates. Assuming a single large hole-like Fermi surface, as measured in strongly overdoped Tl-2201, Hussey has shown that one can calculate the resistivity and Hall coefficient using the Jones-Zener expansion[37]. The model calculates directly the longitudinal and transverse electrical conductivities σ_{xx} and σ_{xy}:

$$\sigma_{xx}=\frac{e^2}{4\pi^3\hbar}\left(\frac{2\pi}{d}\right)4\int_0^{\pi/2}\frac{k_F v_F\cos^2(\varphi-\gamma)}{\Gamma\cos\gamma}\mathrm{d}\varphi$$

$$\sigma_{xy}=\frac{-e^3H}{4\pi^3\hbar^2}\left(\frac{2\pi}{d}\right)4\int_0^{\pi/2}\frac{v_F\cos(\varphi-\gamma)}{\Gamma}\frac{\partial}{\partial\varphi}\left(\frac{v_F\sin(\varphi-\gamma)}{\Gamma}\right)\mathrm{d}\varphi$$

Therefore:

$$R_H=\frac{\sigma_{xy}}{{\sigma_{xx}}^2+{\sigma_{xy}}^2}\frac{1}{H}$$

$$\rho_{xx}=\frac{\sigma_{xx}}{{\sigma_{xx}}^2+{\sigma_{xy}}^2}$$

with e the electron charge, $\hbar$ the reduced Planck constant, d the distance between two CuO_2 planes, k_F the Fermi momentum, v_F the Fermi velocity, φ the angle between the momentum $\boldsymbol{k}$ and the k_x axis in the first Brillouin zone (FBZ), $\gamma(\varphi)=\tan^{-1}\left[\frac{\partial}{\partial\varphi}(\log k_F(\varphi))\right]$, and Γ the scattering rate. Here we choose k_F and v_F not to be φ-dependent, that is, the Fermi surface is a perfect cylinder, implying $\gamma(\varphi)=0$.

We calculate k_F and v_F from hole doping p and effective mass m^* ($=4.1\ m_e$ from quantum oscillations observed in overdoped Tl-2201 (ref. 14)):

$$n=\frac{1+p}{a^2}$$

$$k_F=\sqrt{2\pi n}$$

$$v_F=\frac{\hbar k_F}{m^*}$$

where a is the in-plane lattice constant parameter (we neglect the slight orthorhombicity of YBCO), and n is the carrier density per CuO_2 plane.

Scenario of inelastic scattering applied to YBCO. Here we discuss the possibility that R_H in YBCO at low temperature is enhanced not by a loss of carrier density but by an increase in inelastic scattering.

It has been shown that anisotropic inelastic scattering can increase the value of $R_H(T)$ even if the Fermi surface remains a single large isotropic cylinder[15,37]. This mechanism has been argued to account for the rise in R_H measured in overdoped Tl-2201, as occurs when the doping is decreased from $p=0.3$ to $p=0.27$, for example (Extended Data Fig. 7).

Here we use the following inelastic scattering model developed by Hussey[15], where the effective scattering rate is given by:

$$1/\Gamma(T,\varphi)=1/(\Gamma_0+\Gamma_1\cos^2(2\varphi)T+\Gamma_2T^2)+1/\Gamma_{max}$$

where T is temperature, Γ_0 is the elastic rate scattering coefficient, Γ_1 is the T-linear inelastic scattering rate coefficient, Γ_2 is the T^2 scattering rate, and $\Gamma_{max}=v_F/a$ is the maximum scattering rate limited by the lattice constant a.

Here we use this model to fit our Hall data for YBCO at $p=0.16$, with Γ_1 and Γ_2 the only free parameters (Γ_0 is chosen so that the calculated value of ρ_{xx} at $T=0$ agrees with experiment). The resulting fit is shown in Extended Data Fig. 9c (solid red line). The corresponding curve of $\rho_{xx}(T)=\rho_a(T)$ is plotted in Extended Data Fig. 9d (solid red line).

In Extended Data Fig. 9, we show how these calculated curves vary when the strength of inelastic scattering is varied, both for R_H (Extended Data Fig. 9c) and for ρ_a (Extended Data Fig. 9d). The calculated curves may be compared with experimental curves in YBCO, shown in the left panels of Extended Data Fig. 9, namely R_H versus T in Extended Data Fig. 9a and ρ_a versus T in Extended Data Fig. 9b. We see that by choosing a large value of Γ_1, we can fit the Hall data at $p=0.16$ quite well. The calculated curve drops precipitously below the lowest experimental data point. Then, the decrease in the overall magnitude of R_H versus T with doping can be mimicked in the calculations by decreasing Γ_1 gradually to zero, at which point R_H becomes constant.

However, while the calculated curves for R_H are consistent with the measured Hall data, the calculated curves for ρ_{xx} are in complete disagreement with the measured ρ_a. This is seen by comparing calculated (Extended Data Fig. 9d) and measured (Extended Data Fig. 9b) values. We see that the tenfold increase in the calculated ρ_{xx} at 50 K, caused by the large increase in Γ_1, is not at all observed in

the experimental ρ_a, which are essentially independent of doping at $T = 50$ K. In other words, if inelastic scattering were responsible for the increase in R_H at 50 K with underdoping, it would necessarily show up as a comparable (even larger) increase in the resistivity ρ_a at 50 K. The fact that it does not show up in this way rules out inelastic scattering as a mechanism for the sixfold increase in R_H.

We conclude that the large rise in R_H versus doping is due to a loss of carrier density, and it is a property of the normal-state Fermi surface at $T = 0$.

34. Liang, R., Bonn, D. A. & Hardy, W. N. Growth of YBCO single crystals by the self-flux technique. *Phil. Mag.* **92,** 2563–2581 (2012).
35. Liang, R., Bonn, D. A. & Hardy, W. N. Evaluation of CuO_2 plane hole doping in $YBa_2Cu_3O_{6+x}$ single crystals. *Phys. Rev. B* **73,** 180505 (2006).
36. Gagnon, R., Lupien, C. & Taillefer, L. T^2 dependence of the resistivity in the CuO chains of $YBa_2Cu_3O_{6.9}$. *Phys. Rev. B* **50,** 3458–3461 (1994).
37. Hussey, N. The normal state scattering rate in high-T_c cuprates. *Eur. Phys. J. B* **31,** 495–507 (2003).
38. Manako, T. *et al.* Transport and structural study of $Tl_2Ba_2CuO_{6+\delta}$ single crystals prepared by the KCl flux method. *Phys. Rev. B* **46,** 11019–11024 (1992).
39. Hussey, N. E. *et al.* Angular dependence of the *c*-axis normal-state magnetoresistance in single crystal $Tl_2Ba_2CuO_6$. *Phys. Rev. Lett.* **76,** 122–125 (1996).

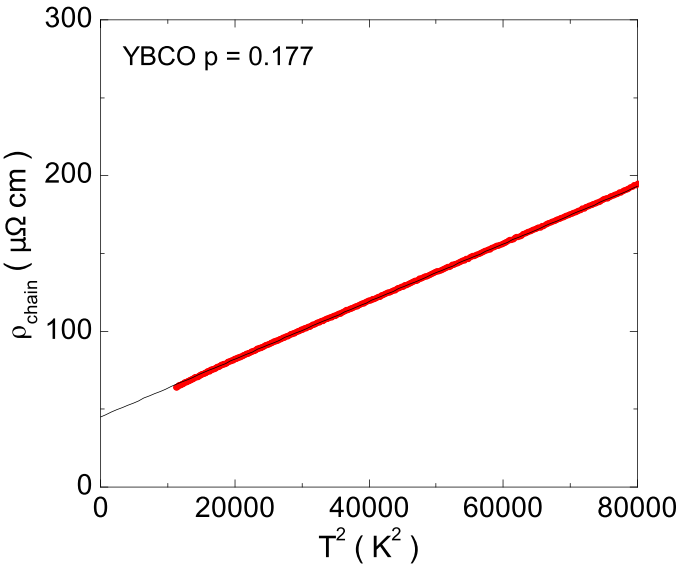

Extended Data Figure 1 | Temperature dependence of resistivity of CuO chains in YBCO at $p = 0.177$. Shown is the chain resistivity in YBCO at $p = 0.177$ (red), defined as $\rho_{chain} = 1/[(1/\rho_b) - (1/\rho_a)]$, where ρ_a and ρ_b are the in-plane resistivities along the a and b directions of the orthorhombic structure, respectively, plotted versus T^2. The black line is a linear fit that extrapolates to $\rho_{chain} = 50\,\mu\Omega\,\mathrm{cm}$ at $T = 50\,\mathrm{K}$.

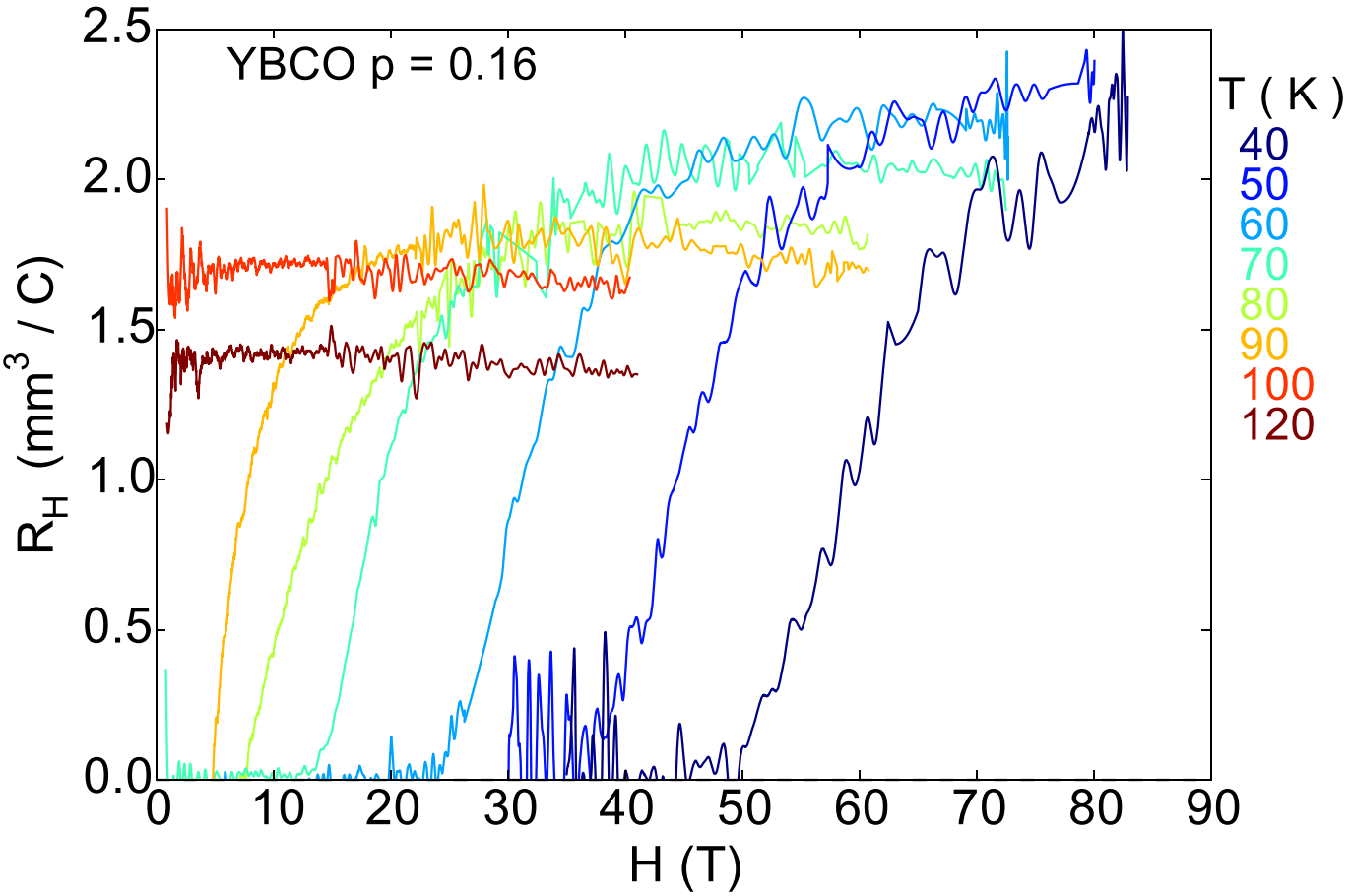

Extended Data Figure 2 | Isotherms of R_H versus H in YBCO at $p = 0.16$. Shown is the magnetic field dependence of the Hall coefficient R_H in our YBCO sample with $y = 6.92$ ($T_c = 93.5$ K; $p = = 0.161$) at various temperatures, as indicated (key at right).

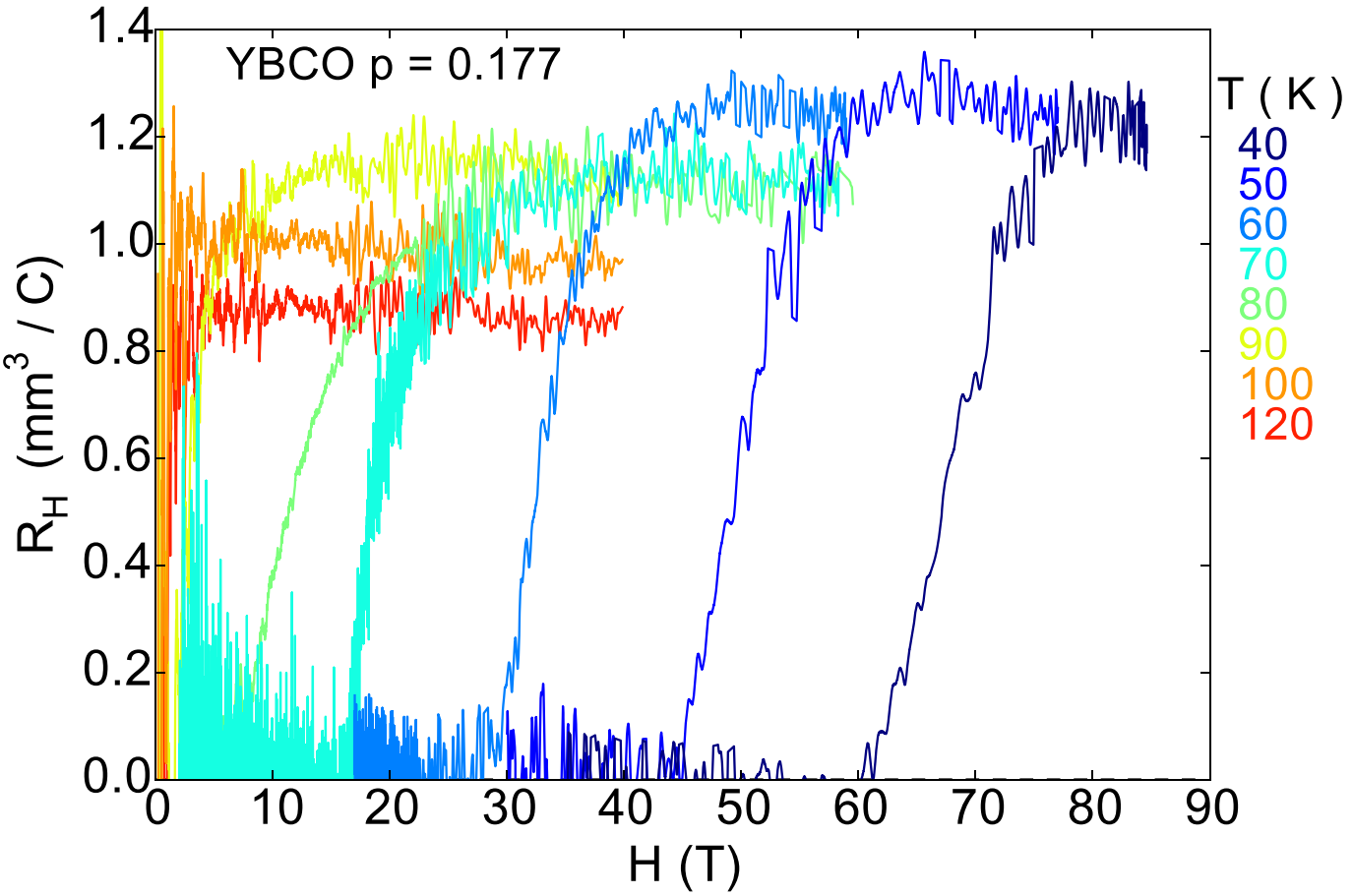

Extended Data Figure 3 | Isotherms of R_H versus H in YBCO at $p = 0.177$. As for Extended Data Fig. 2 but for our YBCO sample with $y = 6.97$ ($T_c = 91$ K; $p = 0.177$).

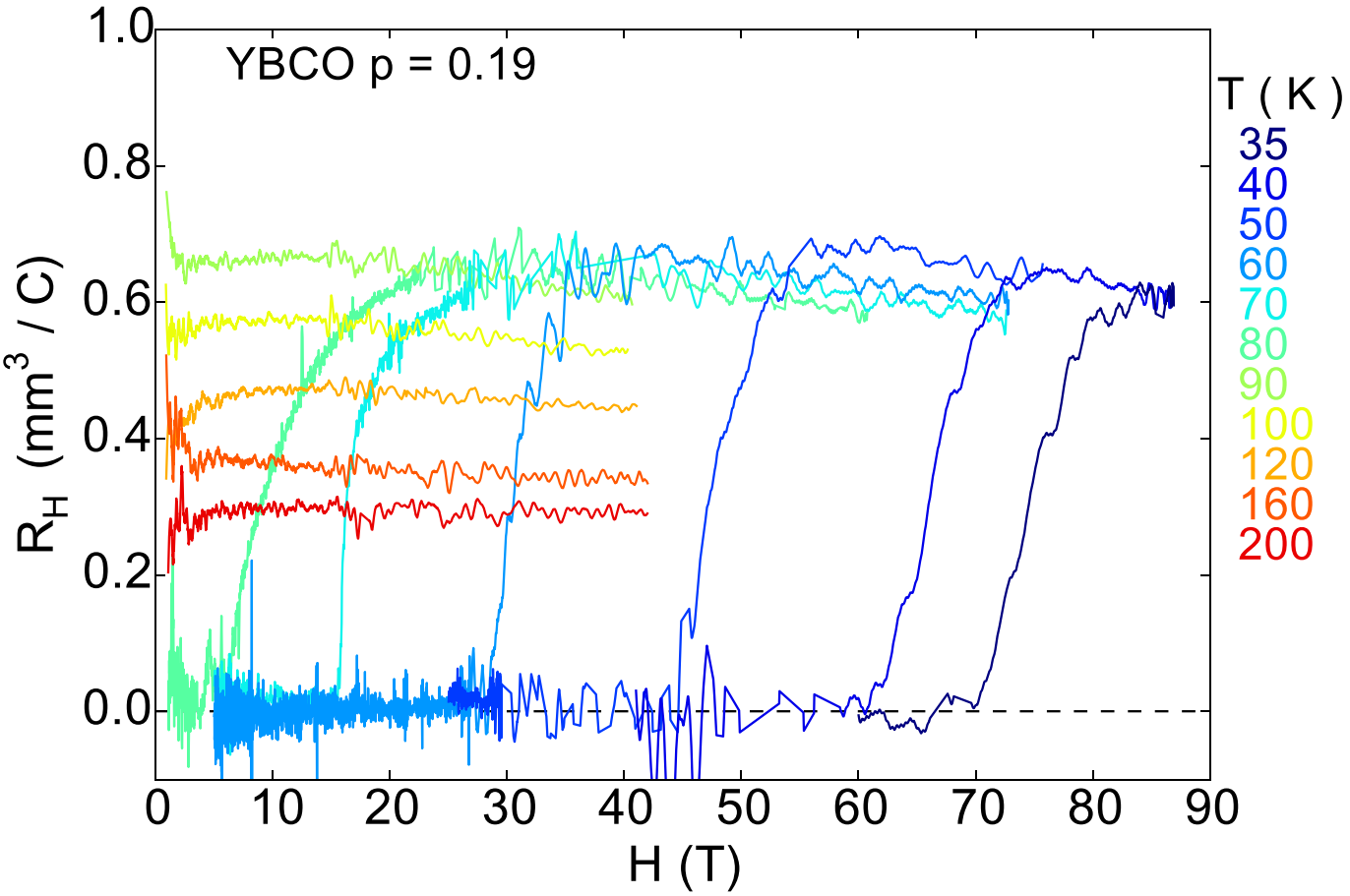

Extended Data Figure 4 | Isotherms of R_H versus H in YBCO at $p = 0.19$. As for Extended Data Fig. 2 but for our YBCO sample with $y = 6.99$ and 1.4% Ca doping ($T_c = 87$ K; $p = 0.19$).

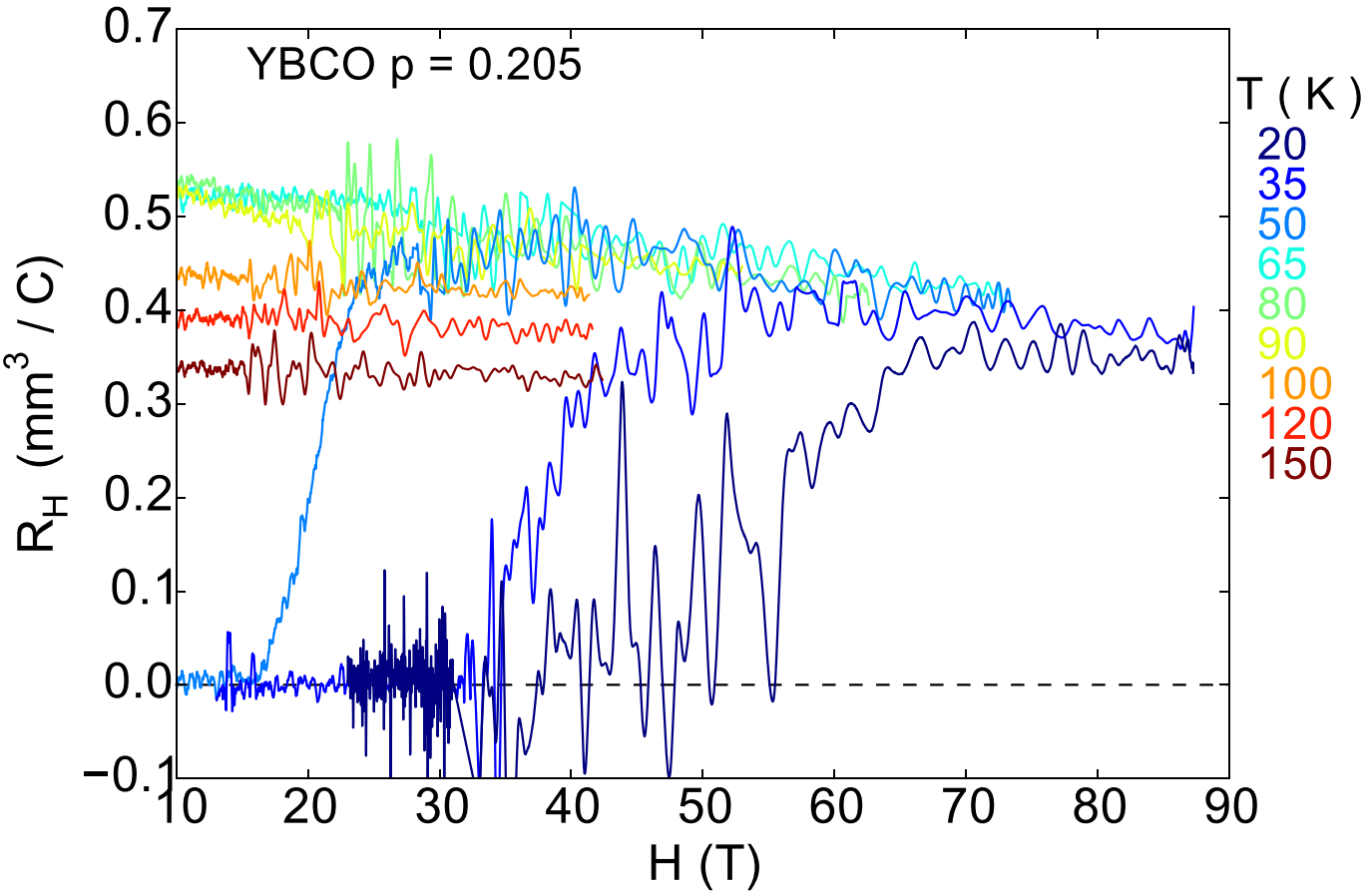

Extended Data Figure 5 | Isotherms of R_H versus H in YBCO at $p = 0.205$. As for Extended Data Fig. 2 but for our YBCO sample with $y = 6.99$ and 5% Ca doping ($T_c = 77$ K; $p = 0.205$).

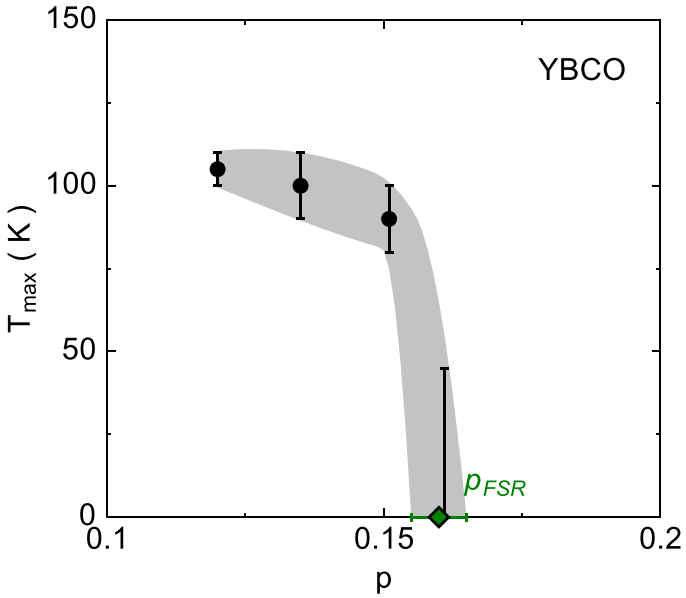

Extended Data Figure 6 | Doping dependence of T_{max}. Shown is the temperature T_{max} at which R_H versus T peaks in YBCO (Fig. 3a), plotted versus doping p. At $p = 0.16$, there is no downturn in the normal-state $R_H(T)$ down to 40 K. The $p = 0.16$ data are consistent with $T_{max} = 0$ (lower bound), with an upper bound at $T_{max} = 40$ K (shown as black vertical segment). The width of the grey band marks the upper and lower limits for T_{max} versus p. The green diamond defines the critical doping above which FSR is no longer present, at $p_{FSR} = 0.16 \pm 0.005$, with an error bar defined from the minimal and maximal possible values of T_{max}. Error bars on the three data points (black dots) represent the uncertainty in defining the peak position of the $R_H(T)$ curves in Fig. 3a.

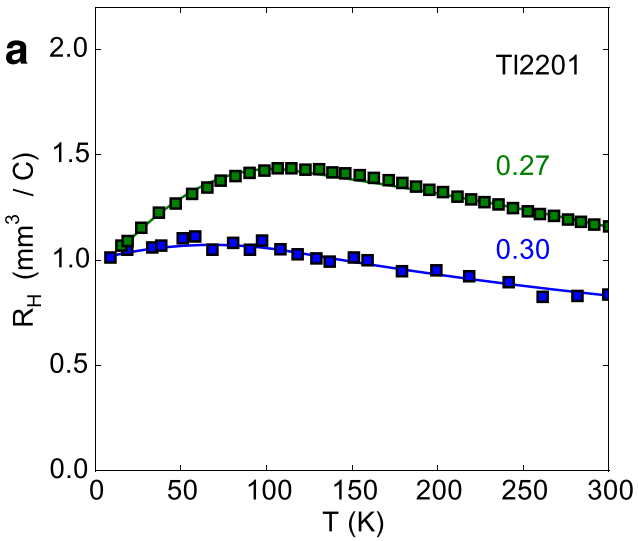

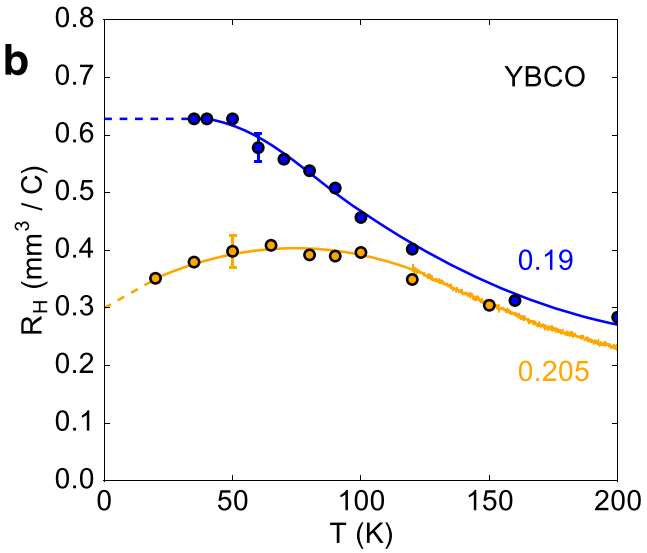

Extended Data Figure 7 | Zoom on R_H versus T in Tl-2201 and YBCO at high doping. a, Temperature dependence of R_H in Tl-2201 (squares) at $p = 0.3$ (blue, $T_c = 10$ K; ref. 38) and $p = 0.27$ (green, $T_c = 25$ K; ref. 39). **b**, R_H versus T in YBCO (circles, from Extended Data Figs 4, 5 and 8) at $p = 0.205$ (yellow) and $p = 0.19$ (blue). The dashed lines are an extrapolation of the low-T data to $T = 0$. The YBCO curve at $p = 0.205$ is qualitatively similar to the two Tl-2201 curves, all exhibiting an initial rise with increasing temperature from $T = 0$, and a characteristic peak at $T \approx 100$ K—two features attributed to inelastic scattering on a large hole-like Fermi surface[15]. The YBCO curve at $p = 0.19$ is qualitatively different, showing no sign of a drop at low T (see Extended Data Fig. 8). We attribute the twofold increase in the magnitude of R_H at $T \to 0$ to a decrease in carrier density as the pseudogap opens at p^*, with p^* located between $p = 0.205$ and $p = 0.19$. The error bars are defined in the legend of Fig. 3.

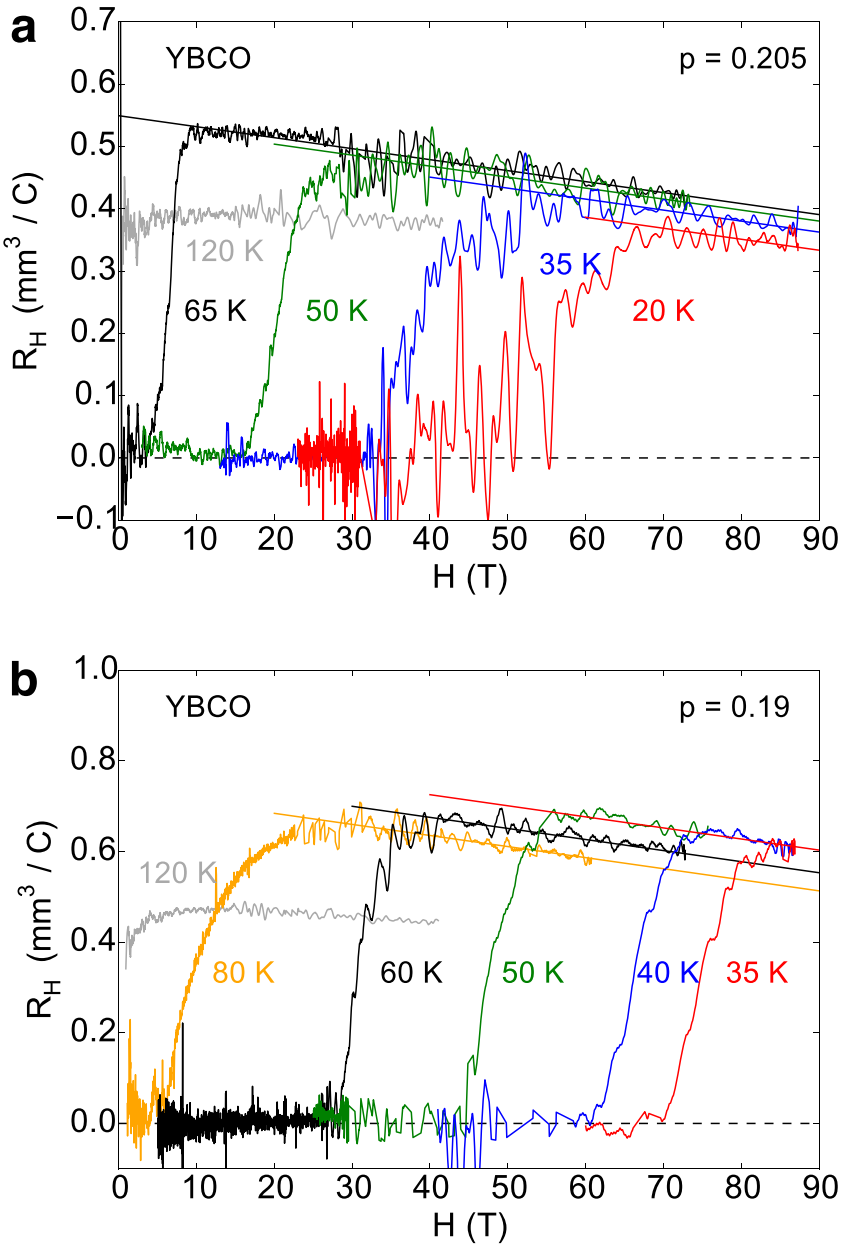

Extended Data Figure 8 | Comparison between $p = 0.205$ and $p = 0.19$. **a**, **b**, The field dependence of the Hall coefficient R_H in YBCO at $p = 0.205$ (**a**) and $p = 0.19$ (**b**), for different temperatures as indicated. The colour-coded lines are parallel linear fits to the high-field data. They show that at low temperature R_H decreases upon cooling at $p = 0.205$, while it saturates at $p = 0.19$. The value of R_H given by the fit line, at $H = 80$ T, is plotted in Fig. 3 and in Extended Data Fig. 7b. Similar fits are used to extract $R_H(80\ \mathrm{T})$ for $p = 0.16$ and $p = 0.177$ (from data in Extended Data Figs 2 and 3).

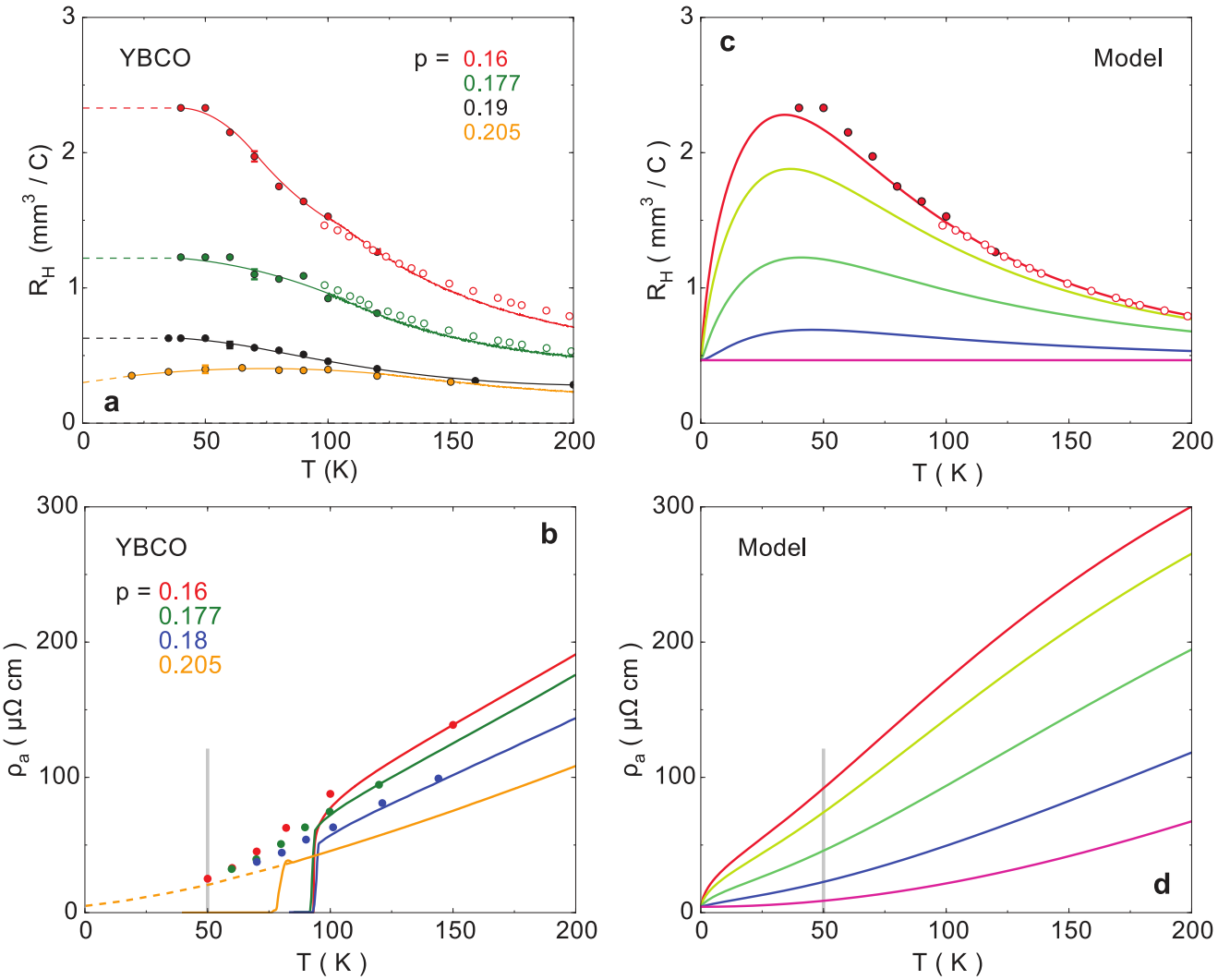

Extended Data Figure 9 | Scenario of inelastic scattering. a, R_H versus T in YBCO at four dopings p, as indicated (Fig. 3b). **b**, Electrical resistivity ρ_a versus T in YBCO at four dopings, as indicated. Lines are at $H = 0$; dots are in the normal state at high field. **c**, R_H versus T calculated for five values of inelastic scattering, with $\Gamma_1 = 0$, 1, 5, 15 and 25 THz K^{-1}, showing that $R_H(T)$ grows with increasing Γ_1 (see Methods). Dots are from **a**. **d**, Corresponding calculated values of the electrical resistivity ρ_a, plotted versus T, using the same parameters and values of Γ_1 as for the colour-coded curves of **c**. The vertical grey lines mark $T = 50$ K, the temperature at which we see a sixfold increase in R_H (**a**), yet no increase in ρ_a (**b**). The calculation can reproduce the large increase in R_H (**c**), but it is accompanied by a tenfold increase in ρ_a (**d**).

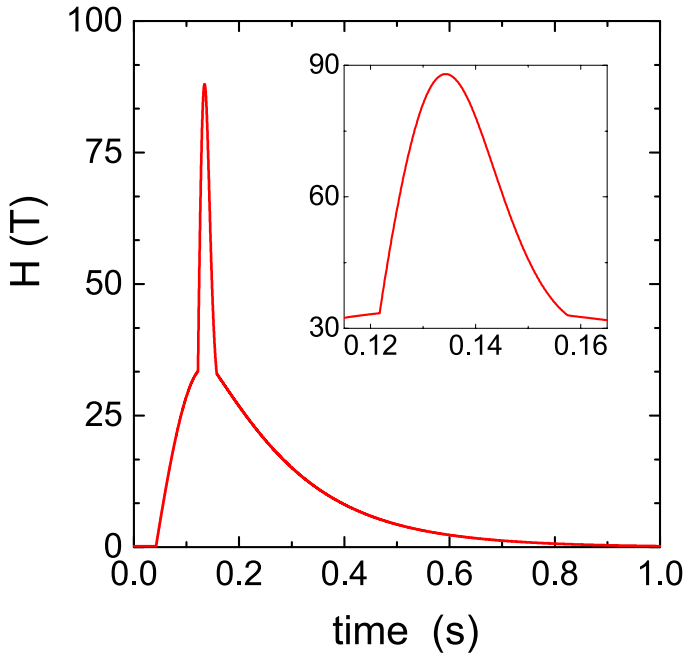

Extended Data Figure 10 | Magnetic field profile. Time dependence of the magnetic field pulse in the 90 T dual-coil magnet at the LNCMI in Toulouse. Inset, zoom around maximum field.